

Article

Optimal Wireless Power Transfer Circuit without a Capacitor on the Secondary Side

Sabriansyah Rizqika Akbar ^{1,*}, Eko Setiawan ¹, Takuya Hirata ² and Ichijo Hodaka ^{3,*}

¹ Informatics Engineering Department, Faculty of Computer Science, University of Brawijaya, Malang 65145, Indonesia; ekosetiawan@ub.ac.id

² Department of Electronic Mechanical Engineering, National Institute of Technology, Oshima College, Yamaguchi 742-2193, Japan; hirata@oshima-k.ac.jp

³ Department of Environmental Robotics, Faculty of Engineering, University of Miyazaki, Miyazaki City 889-1692, Japan

* Correspondence: sabrian@ub.ac.id (S.R.A.); hijhodaka@cc.miyazaki-u.ac.jp (I.H.)

Abstract: This study proposes an approach to obtain maximum power via wireless power transfer using a single primary-side capacitor. It is shown that higher power is achieved when compared to the common wireless power transfer circuit under resonance with dual (primary- and secondary-side) capacitors. This approach is divided into three phases. By choosing the capacitor and frequency as freely assignable variables, we symbolically obtain a formula that allows us to determine the optimized capacitance and frequency for maximum power. To verify our method, we used a numerical analysis and compared it with an electronic circuit simulation. The symbolic formula is able to maintain maximum power despite changes in load or in the coupling coefficients.

Keywords: wireless power transfer; resonance; maximum power



Citation: Akbar, S.R.; Setiawan, E.; Hirata, T.; Hodaka, I. Optimal Wireless Power Transfer Circuit without a Capacitor on the Secondary Side. *Energies* **2023**, *16*, 2922. <https://doi.org/10.3390/en16062922>

Academic Editor: Abu-Siada Ahmed

Received: 20 January 2023

Revised: 23 February 2023

Accepted: 6 March 2023

Published: 22 March 2023



Copyright: © 2023 by the authors. Licensee MDPI, Basel, Switzerland. This article is an open access article distributed under the terms and conditions of the Creative Commons Attribution (CC BY) license (<https://creativecommons.org/licenses/by/4.0/>).

1. Introduction

The Tesla coil and Tesla Tower's introduction in the early 20th century triggered the research on wireless power transfer (WPT) [1]. Nicola Tesla was able to light a light bulb held barehanded within a certain distance of the Tesla Tower. In the last decade, the demand for electronic handheld and compact devices (mobile phones, laptops, tablets, etc.) has increased, which led Massachusetts Institute of Technology (MIT) researchers in 2007 to introduce a wireless power transfer method called strong magnetic coupling resonances [2]. The researchers of this paper were able to deliver power to a 60 W light bulb at a distance of 2 m. The research and development of WPT technology are currently ongoing, and are nearing a standardization and commercialization phase. Currently, WPT technology can supply charges to electronic handheld devices, autonomous devices, and electric vehicles.

WPT technology utilizes electromagnetic fields to transmit power to the receiver, which can be accomplished through various methods, including inductive WPT, capacitive WPT [3], radio frequency [4], and laser [5]. Inductive and capacitive WPTs are particularly effective for delivering power over short distances [6]. Currently, researchers studying WPT are developing a system with better distance, better power, and better efficiency [7–10]. At present, WPT research is focused on exploring the system architecture and optimization design [11]. The most basic circuit for making a WPT system uses a voltage source and coils in the primary and secondary circuit [12]. The current through the coils enables a magnetic field around the coils and creates self-inductance and mutual inductance between the coils [13]. However, this minimum WPT circuit delivers a smaller amount of power compared to a direct connection. Therefore, to increase the amount of power absorbed by the load, an additional inductor or capacitor is needed in the primary or secondary circuit, or in both. This method is known as the compensation technique [14,15].

The coil design is an essential factor in the WPT circuit [16,17], since it influences the parasitic resistances. High parasitic resistance can decrease the transmitted power, while low parasitic resistance leads to increased power and high efficiency [18]. Thus, researchers want to reduce or even eliminate the effect of the coils' parasitic resistance on the primary and secondary side by designing a WPT system that works at the resonant frequency. Hence, the L (coil) and C (capacitor) pair component is mainly used on the primary side and secondary side to form the series-series (SS), series-parallel (SP), parallel-series (PS), and parallel-parallel (PP) WPT circuits [19]. Researchers have explored the optimal operating points to find the best transfer efficiency or best power by analyzing and avoiding the frequency splitting issues. Frequency splitting is a WPT phenomenon where the peak divides if the coupling coils are greater than the critical coupling [20]. Therefore, if frequency splitting occurs, the inductance, capacitance, or distance needs to be optimized for better power delivery [21]. Current research on WPT optimization has been reviewed in [22]. The optimization approach has been applied in various methods, such as impedance matching [23–25], parameter optimization [26,27], and the use of artificial intelligence [28,29].

Since research on series WPT circuits usually focuses on the dual-capacitor circuit, the single-capacitor circuit is under evaluated and under reviewed. This circuit can be considered a simple compensation circuit, since there is no capacitor on the secondary side. Finding the resonant frequency operations in this circuit is challenging, since it only has a primary-side capacitor. Therefore, the question regarding what will happen if we omit the capacitor on the secondary side needs to be answered.

This study proposes carrying out an optimization approach in a primary-side single-capacitor WPT circuit to obtain high-power WPT. This study focuses on the formal methods by compensating for the circuit with the optimum point of the capacitor and frequency. The maximum power objective function is calculated from the steady-state analysis process. Furthermore, a formula determining the optimum points from the capacitor and frequency values is presented. By choosing the capacitor and the frequency value as the optimum points, we also prove that the optimal condition can be maintained, even when there is a change in the system coupling coefficient or load.

2. Methods

The proposed approach (Figure 1) consists of three phases: a system model, a steady-state analysis, and an optimization phase. The system model formulizes the transfer function from the primary-side single-capacitor circuit. The state-space variables are obtained corresponding to the input and output definition using Kirchhoff's circuit law. Next, the state-space matrix is formed and calculated using the state-space equation to obtain the system transfer function [30]. The second phase consists of analyzing the system's steady-state conditions. In this phase, a steady-state function is obtained by considering the input signal and the system transfer function. The last phase is the optimization phase, which maximizes the objective function obtained from the steady-state equation. A partial derivative from the objective function, with respect to the capacitor and frequency, was obtained. The solutions from the simultaneous partial derivative equation produce an optimum point capacitor and a frequency equation. The function of the maximal power is obtained by substituting both optimum point equations with an objective function.

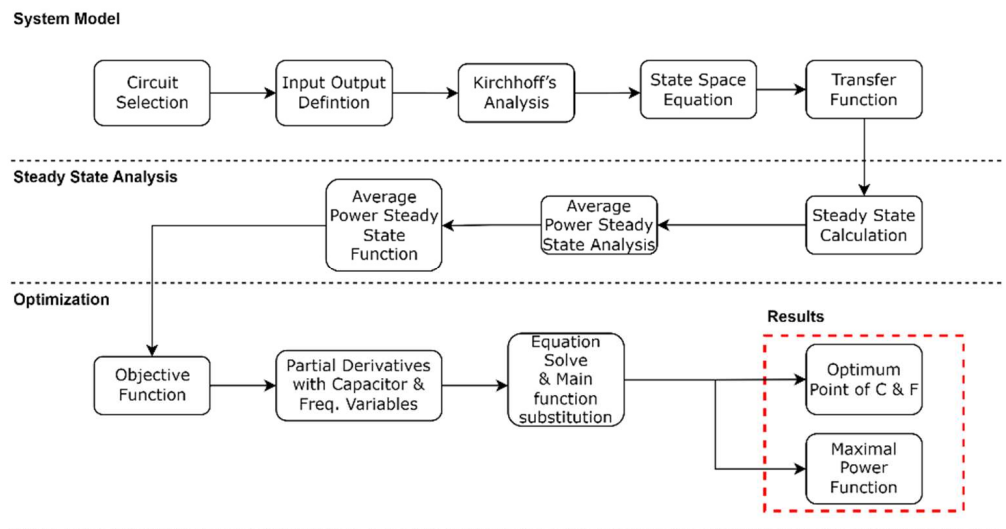


Figure 1. Optimization approach consists of system model, steady-state analysis, and optimization phases.

2.1. Circuit Topologies of Wireless Power Transfer

Figure 2a is a schematic of the most popular series type of WPT circuit, where the WPT circuit transfer power originates at the power source on the primary side to load R_L on the secondary side. A couple of inductors (L_1 and L_2) are necessary to realize wireless power transfer using an electromagnetic field. The circuit is compensated with capacitors on both sides to apply the idea of resonance, as is shown in Figure 2a. Figure 2b shows a schematic of the series connection type of the WPT system, where the capacitor C_2 on the secondary side is omitted. We cannot simply use the idea of resonance because of the lack of symmetry. Instead, we will optimize circuit component parameters to obtain the maximal power at the load R_L independent of resonance. The primary circuit consists of an input voltage source (u) with an internal resistance (R_s), a capacitor (C), the transmitter inductor (L_1), and the internal resistance (R_1). The secondary circuit consists of the receiver inductor (L_2) with its internal resistance (R_2) and the load (R_L). Let M and K be the mutual inductance and coupling coefficients between the transmitter and receiver inductors, which can be replaced by Equation (1).

$$K = \frac{M}{\sqrt{L_1 L_2}} \tag{1}$$

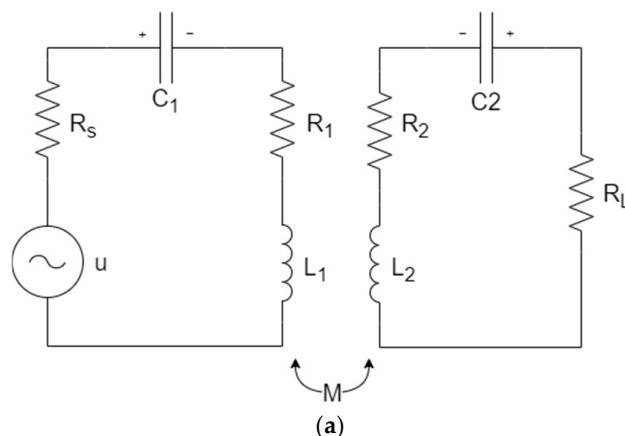


Figure 2. Cont.

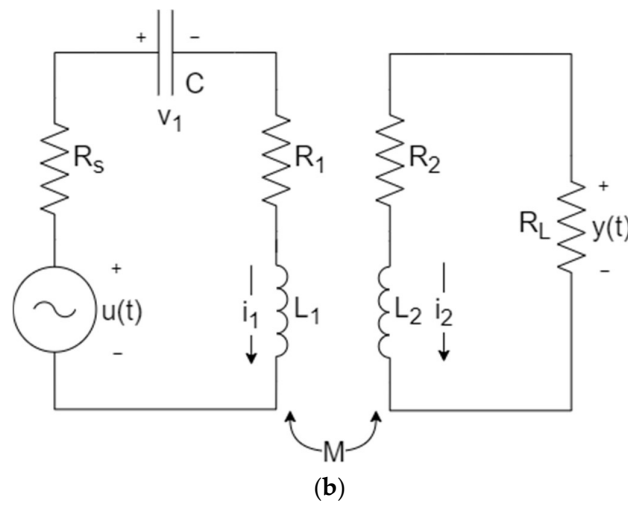


Figure 2. (a) The most common dual-capacitor WPT circuit; (b) proposed single-capacitor circuit.

2.2. Circuit Equation

We will analyze the wireless power transfer circuit in Figure 2b. Let us start with the circuit equation in the form of Equation (2).

$$\frac{dv_1}{dt} = \frac{i_1}{C}$$

$$\frac{di_1}{dt} = \frac{-L_2(R_1i_1 + R_Si_1 - u + v_1) + Mi_2(R_2 + R_L)}{L_1L_2 - M^2} \tag{2}$$

$$\frac{di_2}{dt} = \frac{-L_1i_2(R_2 + R_L) + M(R_1i_1 + R_Si_1 - u + v_1)}{L_1L_2 - M^2}$$

where $v_1, i_1,$ and i_2 are state-space variables, u is the input, and y is the output. Equivalently, we define our state-space representations as Equation (3).

$$\begin{aligned} \dot{x} &= Ax + Bu \\ y &= Cx + Du \end{aligned} \tag{3}$$

where

$$A = \begin{bmatrix} 0 & \frac{1}{C} & 0 \\ -\frac{L_2}{L_1L_2 - M^2} & \frac{-L_2R_1 - L_2R_S}{L_1L_2 - M^2} & \frac{MR_2 + MR_L}{L_1L_2 - M^2} \\ -\frac{M}{-L_1L_2 + M^2} & \frac{-MR_1 - MR_S}{-L_1L_2 + M^2} & \frac{L_1R_2 + L_1R_L}{-L_1L_2 + M^2} \end{bmatrix}, B = \begin{bmatrix} 0 \\ \frac{L_2}{L_1L_2 - M^2} \\ \frac{M}{-L_1L_2 + M^2} \end{bmatrix} \tag{4}$$

$$C = [0 \quad 0 \quad -R_L], D = 0$$

$$x = \begin{bmatrix} v_1 \\ i_1 \\ i_2 \end{bmatrix} \tag{5}$$

The transfer of Function (2) from u to y is given by

$$G(s) = C(sI - A)^{-1}B + D$$

$$= \frac{CMR_L s^2}{R_2 + R_L + s^3(CL_1L_2 - CM^2) + s^2(CL_1R_2 + CL_1R_L + CL_2R_1 + CL_2R_S) + s(CR_1R_2 + CR_1R_L + CR_2R_S + CR_LR_S + L_2)} \quad (6)$$

2.3. Steady-State Function

Our circuit equation stimulated by a periodic input has a periodic solution where the period is the same as the input since the differential equation is a linear time-invariant system. If the system is stable, i.e., all the eigenvalues of matrix A have a negative real part, then the periodic solution will be asymptotically stable. In other words, any solution starting with any initial value will behave as the periodic solution when enough time has passed; thus, the periodic solution is often called a steady-state solution [31]. In the beginning, it is important to obtain the steady-state function to obtain the exact calculation under the steady-state conditions [32,33]. In this computation, we use the symbolic computation [34] of the $y(t)$ output, described as $y_{ss}(t)$. A similar approach was also conducted by [35] to perform the time domain analysis and modeling before the optimization process. Since this study analyzes the circuit's behavior using the sine wave input, the input function $u(t)$ can be described as Equation (7), where u_0 is the amplitude of the input voltage.

$$u(t) = u_0 \sin(\omega t) \quad (7)$$

From the sinusoidal input of Equation (7), the steady-state function of $y_{ss}(t)$ can be described by Equation (8) [36].

$$y_{ss}(t) = u_0 |G(j\omega)| \sin(\omega t + \angle G(j\omega)) \quad (8)$$

$p_{ss}(t)$ is the power at the load R_L in the steady state. The average of $p_{ss}(t)$ over a period is called the average power at the load R_L . From Equations (8) and (9), the average power can be calculated using Equations (9)–(11).

$$p_{ss}(t) = \frac{y_{ss}(t)^2}{R_L} \quad (9)$$

$$p_{ss} = \frac{1}{T} \int_{t_0}^{t_0+T} \frac{y_{ss}(t)^2}{R_L} dt \quad (10)$$

$$p_{ss} = \frac{|G(j\omega)|^2}{2R_L T} \int_{t_0}^{t_0+T} (1 - \cos 2(\omega t + \angle G(j\omega))) dt \quad (11)$$

$$p_{ss} = \frac{|G(j\omega)|^2}{2R_L}$$

2.4. Objective Function and Optimization

Most research obtains a high power level at load R_L by calculating the capacitor and frequency values using the resonant calculation, given by Equation (12). This resonant calculation is generally used for common WPT dual-capacitor circuits (Figure 2a). However, this resonant calculation cannot be used with our proposed circuit (Figure 2b) since it only contains a single capacitor, and thus, it lacks symmetry. Therefore, in this section, we propose a method to obtain a high-power level by finding the optimum point of the capacitor and frequency values for $p_{ss}(t)$.

$$f = \frac{1}{2\pi\sqrt{L_1C_1}} = \frac{1}{2\pi\sqrt{L_2C_2}} \quad (12)$$

As in Equation (9), the $p_{ss}(t)$ equation contains the $y_{ss}(t)$ equation, as in Equation (8). The $y_{ss}(t)$ equation is linear with $G(j\omega)$, which is our obtained transfer function from

Equation (6). Hence, $p_{ss}(t)$ is affected by many parameters, which include the input voltage from the voltage source (u_0) and its internal resistance (R_S), the coils (L_1 and L_2) and their parasitic resistance (R_1 and R_2), the coupling coefficient (K), the capacitor value (C), the frequency (ω), and the load resistor (R_L). Then, we can conduct the optimization and simplify the computation by noticing the design considerations described as follows:

1. The voltage from the voltage source (u_0) is at a constant value and has a fixed internal resistance (R_S). Therefore, as we see in Equations (8) and (9), u_0 has a linear relationship with the load power $p_{ss}(t)$.
2. Designing and fabricating the coil will affect its parasitic resistance [18]. Accordingly, it is important to consider the fixed proportional change of the coil resistance (R_1 and R_2) that depends on the coils L_1 and L_2 .
3. The coupling coefficient (K) depends on the mutual inductance (M) and the value of the L_1 and L_2 coils. In addition, the transfer distance between the coils affects the K value [16,18].
4. The most suitable way to gain a high-power level during the charging process is by changing the capacitor and frequency, as shown in [23,25].

Therefore, to simplify $G(j\omega)$, we introduce new variables as described in Equation (13). We introduce the α_1 and α_2 variables as a constant ratio between the coil and its parasitic resistance.

$$\alpha_1 = L_1/R_1 \quad \alpha_2 = L_2/R_2 \quad \alpha_S = L_1/R_S \quad \alpha_L = L_2/R_L \quad Q = CR_S \quad (13)$$

At this point, the optimization is conducted with the objective function $F = \frac{|G(j\omega)|^2}{R_L}$. Let (Q^*, ω^*) be the optimum point on $F(Q, \omega)$, and then this point holds for Equation (14).

$$\begin{cases} \frac{\partial F}{\partial Q}(Q^*, \omega^*) = 0 \\ \frac{\partial F}{\partial \omega}(Q^*, \omega^*) = 0 \end{cases} \quad (14)$$

By solving Equation (14), we obtain Q^* and ω^* as in Equations (15) and (16).

$$Q^* = \frac{\alpha_2^2 \alpha_L^2 \omega^2 + \alpha_2^2 + 2\alpha_2 \alpha_L + \alpha_L^2}{\alpha_S \omega^2 (-K^2 \alpha_2^2 \alpha_L^2 \omega^2 + \alpha_2^2 \alpha_L^2 \omega^2 + \alpha_2^2 + 2\alpha_2 \alpha_L + \alpha_L^2)} \quad (15)$$

$$\omega^* = \frac{\sigma \sqrt{\alpha_1 + \alpha_S} (\alpha_2 + \alpha_L)}{\sqrt{\alpha_2} \sqrt{\alpha_L}} \quad (16)$$

Finally, by substituting Equations (15) and (16) with F , we obtain the maximum function as described in Equation (17).

$$F(Q^*, \omega^*) = \frac{K^2 \alpha_1^2 \alpha_2 \alpha_S \beta \sigma^2 (\alpha_2 (\alpha_1 \alpha_L \sigma^2 + \alpha_L \alpha_S \sigma^2) + 1)}{R_L (\alpha_1 + \alpha_S) (\alpha_1 (K^2 (\alpha_2 \alpha_S \sigma^2 + \alpha_L \alpha_S \sigma^2) + \alpha_2 \alpha_L \sigma^2) + \alpha_2 \alpha_L \alpha_S \sigma^2 + 1)^2} \quad (17)$$

where $\sigma = \frac{1}{\sqrt{|-K^2 (\alpha_1 \alpha_2 \alpha_S + \alpha_1 \alpha_L \alpha_S) + \alpha_1 \alpha_2 \alpha_L + \alpha_2 \alpha_L \alpha_S|}}$

3. Verification and Simulation Results

We used the Simulation Program with Integrated Circuit Emphasis (SPICE) software to verify our method. We demonstrated our computation using the circuit topology, as shown in Figure 2b. The component value was taken from [21] using the 1-volt constant voltage input from the voltage source, which is shown in Table 1.

Table 1. Circuit component configuration.

L_1	L_2	R_1	R_2	R_S	R_L	K
25.2 μ H	25.2 μ H	0.73 Ω	0.73 Ω	1 Ω	100 Ω	0.08

Next, we setup the simulation environment to verify our steady-state function, average power, and results obtained from our proposed optimization.

3.1. Steady-State Analysis

The steady-state analysis aims to show whether our proposed WPT system, shown in Figure 2b, is stable and has a periodic (steady-state) solution when enough time has passed. Therefore, we can use our steady-state functions $y_{ss}(t)$ (Equation (8)) and $p_{ss}(t)$ (Equation (9)) to obtain steady-state voltage and R_L power without waiting for the transient response. A system’s state-space complete response (solutions) can be described by Equation (18), where the first term in the equations of $x(t)$ and $x'(t)$ is the initial response, while the second is the steady-state response. $x(0)$ is a vector taken from the state-space variables v_1 (capacitor voltage), i_1 (primary coil current), and i_2 (secondary coil current) in Equation (5).

$$\begin{aligned}
 x(t) &= e^{At}x(0) + \int_0^t e^{-Ap}Bu(p)dp \\
 x'(t) &= e^{At}(x(0) - \int_{-\infty}^0 e^{-Ap}Bu(p)dp) + e^{At}\int_{-\infty}^t e^{-Ap}Bu(p)dp
 \end{aligned}
 \tag{18}$$

Hence, to obtain a representation from our proposed steady-state function and show the steady-state conditions from our system, we compared the $y_{ss}(t)$ and $p_{ss}(t)$ computations with SPICE simulations. The simulations were performed on our proposed circuit in Figure 2b and the components were configured as in Table 1. At this step, we calculated the frequency (f) and capacitor (C) using the resonant frequency from the primary circuit described in Formula (19).

$$f = \frac{1}{2\pi\sqrt{L_1C}}
 \tag{19}$$

Using Formula (19), we calculated $C = 0.1 \mu$ F to obtain the resonant frequency of 100 kHz. The transient analysis simulations were ran with intervals of 0–0.3 ms using a 1 V sine wave input. The simulations were configured by giving the $x(0)$ initial conditions a random value, which is defined in Table 2.

Table 2. Steady-state analysis simulation setup.

Simulation Setup	Initial Condition		
	v_1	i_1	i_2
1	15 V	0 mA	0 mA
2	0 V	0.3 mA	0 mA
3	20 V	0 mA	0 mA
4	0 V	0.15 mA	0 mA

We plotted the transient simulation results for the R_L voltage and compared them to the $y_{ss}(t)$ model in Figure 3. The first setup results represented in Figure 3a show the unsteady R_L voltage when the initial condition of 15 volts is given to the capacitor. The R_L voltage begins to steady after 0.1 ms. When the 0.3 mA initial condition is given to L_1 (setup 2), the unsteady behavior occurs at the beginning from 0 to 0.9 ms, as shown in Figure 3b. Results from Figure 3 show that, under the steady-state condition, the $y_{ss}(t)$ model gives similar values compared to the simulation. Therefore, $y_{ss}(t)$ is a stable solution.

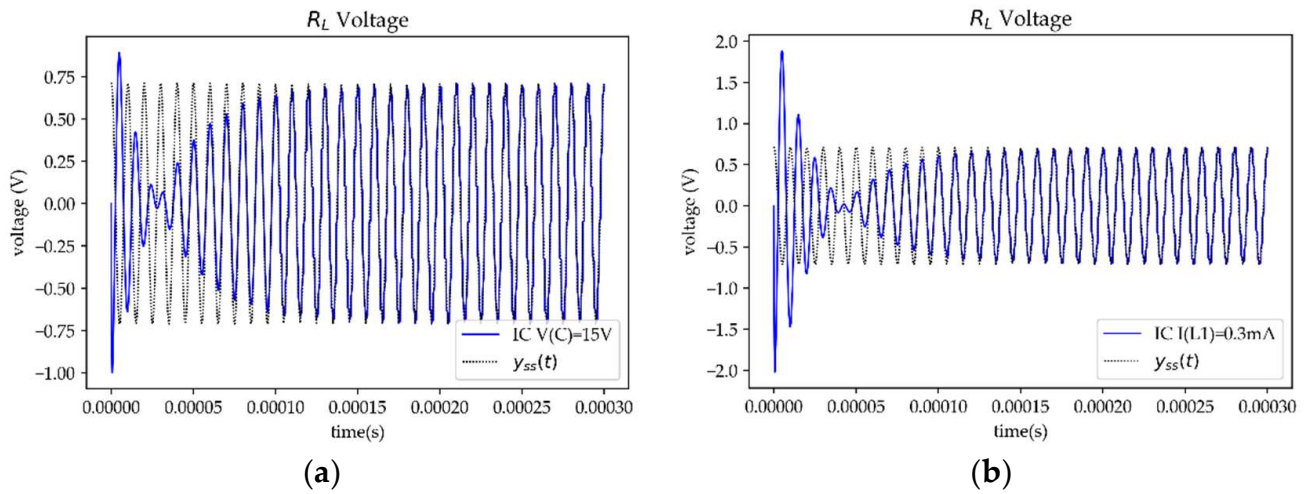


Figure 3. R_L voltage transient simulation results compared to $y_{ss}(t)$ calculations from Equation (8): (a) using 15 V initial condition at capacitor; (b) using 0.3 mA initial condition at primary-side coil (L_1).

The comparison of $p_{ss}(t)$ with the SPICE transient simulation result is presented in Figure 4. The initial condition given to the capacitor (setup 3) and L_1 (setup 4) generates unsteady behavior at the beginning of the simulations. However, when the time reaches 0.3 ms, the simulation result shows that the system began to reach the steady-state condition, and it has similar outputs with the $p_{ss}(t)$ calculations. Therefore, the steady state's average power calculations can be obtained using $p_{ss}(t)$, since this function shows the stable solution.

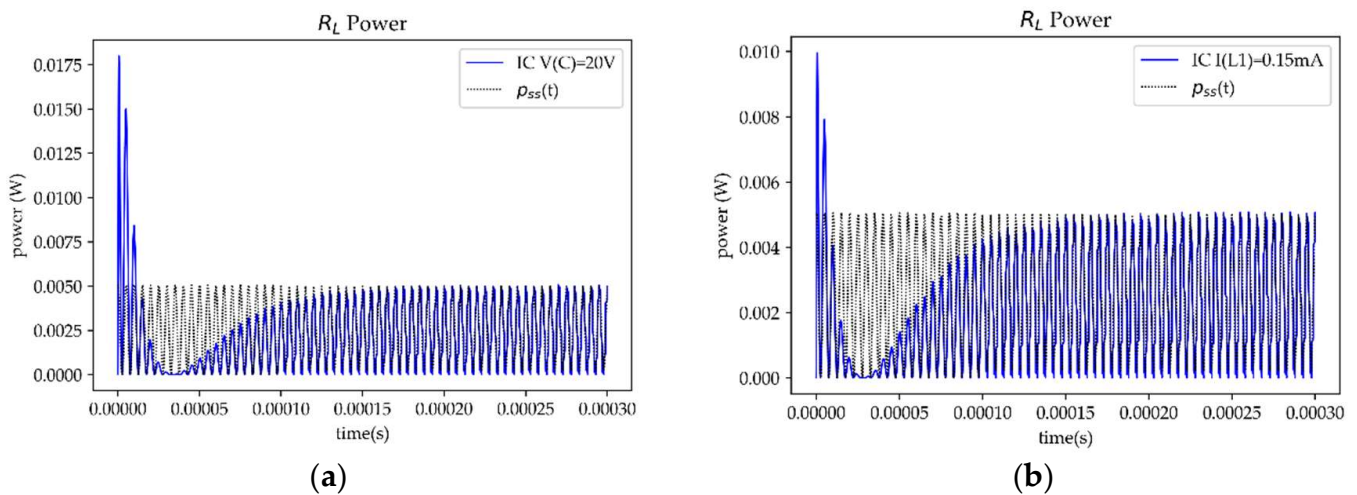


Figure 4. R_L power transient simulation results compared to $p_{ss}(t)$ calculations from Equation (12): (a) using 20 V initial condition at capacitor; (b) using 0.15 mA initial condition at primary-side coil (L_1).

3.2. Comparison of Average Power at the Load R_L between the Unoptimized and the Optimized Capacitor Frequency Values

This section compares the unoptimized and optimized average power calculations for our single-capacitor circuit, shown in Figure 2b. First, the component value is set using the values in Table 1. Then, for the unoptimized condition, the capacitor and frequency values are calculated using the primary-side resonant frequency from Formula (19). Therefore, we obtained $C = 0.1 \mu\text{F}$ and the frequency 100 kHz. Then, using Equations (8) and (9), we computed and plotted $y_{ss}(t)$ and $p_{ss}(t)$ in Figure 5. From Equations (10) and (11), the average power calculations were obtained as 2.5 mW.

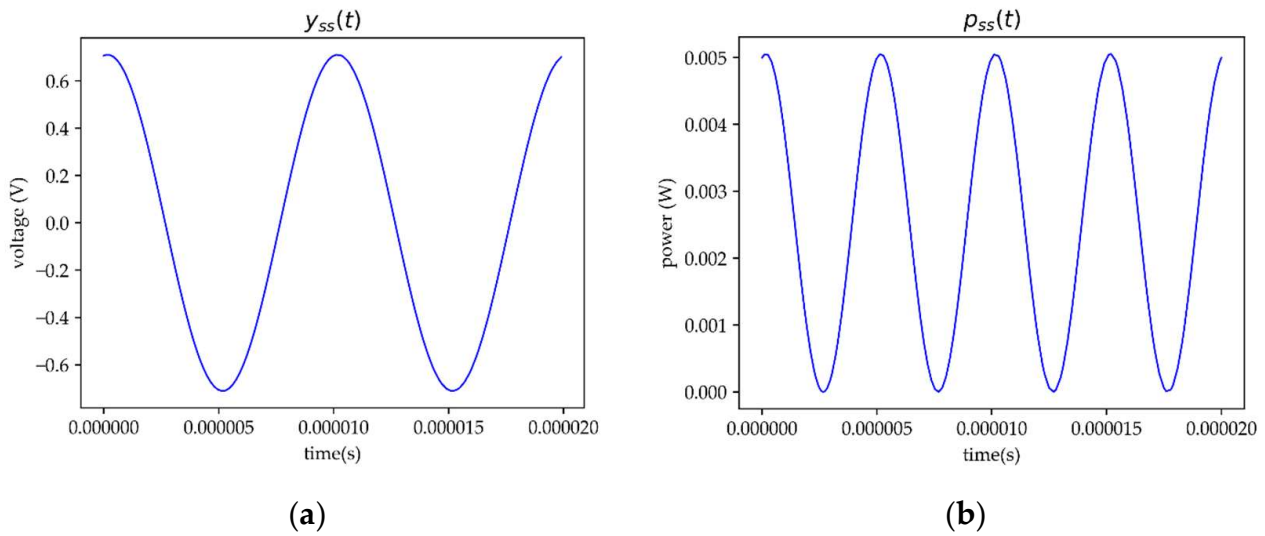


Figure 5. (a) Unoptimized $y_{ss}(t)$ and (b) unoptimized $p_{ss}(t)$ function transient analysis ranging from 0 to 20 μ s.

Next, we optimized the capacitor and frequency values (C - f) using our proposed method to obtain Q^* and ω^* as in Equations (15) and (16). The calculation shows that $\omega^* = 5.046 \times 10^6$ rad/s. From ω^* , the frequency was obtained at 803.6 kHz. Afterward, we substituted the ω^* value into Equation (15) to obtain $Q^* = 1.56 \times 10^{-9}$, since $Q = CR_S$ as mentioned in Equation (13), and $R_S = 1 \Omega$. Then, the C value was found to be equal to 1.56 nF. Using this optimal C - f value, we computed and plotted $y_{ss}(t)$, and $p_{ss}(t)$, as presented in Figure 6. The average power obtained from the calculations of Equations (10) and (11) was 0.043 Watts. By comparing the unoptimized condition in Figure 5 and the optimized condition in Figure 6, we determined that the load's average power R_L improved significantly after C - f was optimized.

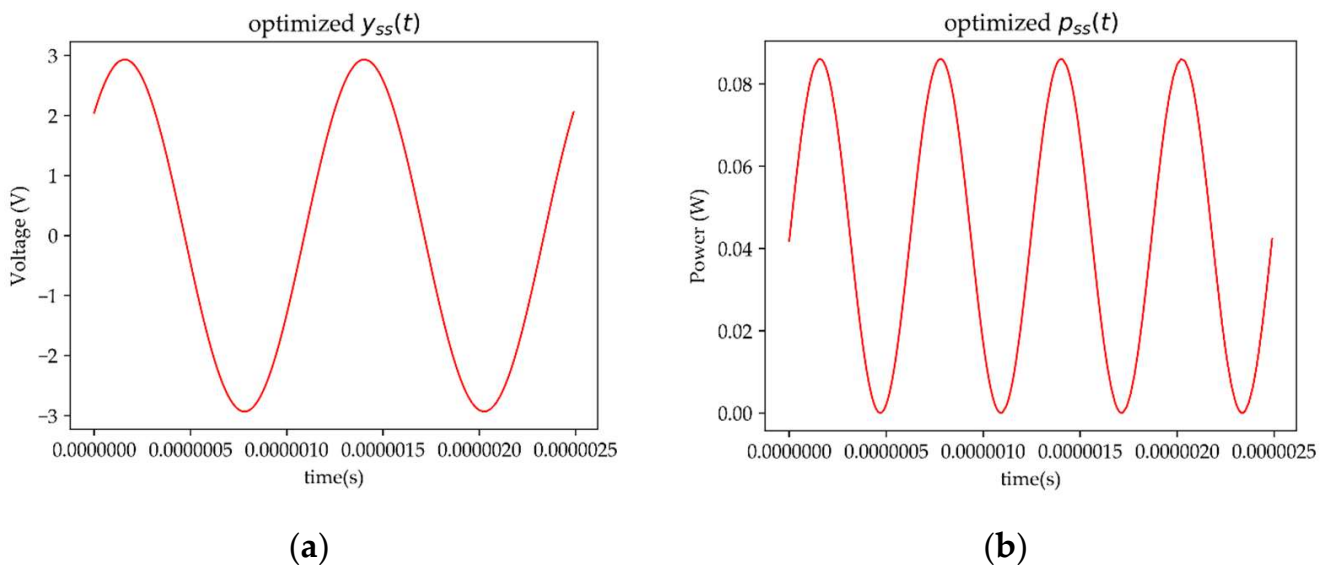


Figure 6. (a) Optimized $y_{ss}(t)$ and (b) optimized $p_{ss}(t)$ function transient analysis ranging from 0 to 25 μ s.

3.3. Comparison of Power at the Load R_L between Optimized Single-Capacitor and Dual-Capacitor Resonant Calculations

To verify that our proposed design method can obtain a high-power level that is high enough compared to the resonant calculations (even if the circuit loses symmetry and not using the idea of resonance), we performed SPICE simulations using the scenarios as follows:

1. Single-capacitor WPT circuit (Figure 2b) using the idea of primary-circuit resonance for $C-f$ from Equation (18).
2. Single-capacitor WPT circuit (Figure 2b) with an optimized $C-f$ condition using the proposed Formulas (15) and (16).
3. Common dual-capacitor WPT circuit (Figure 2a) using the idea of primary-circuit resonance for $C-f$ from Equation (12).

The SPICE simulation uses each circuit’s environment setup, shown in Figure 2, and the fundamental component values, presented in Table 1. Since our proposed formula in scenario 2 introduces new variables, we converted the component values in Table 1 into those presented in Table 3 using Equation (13). At the same time, the $C-f$ method calculation for each scenario is described in Table 4.

Table 3. Variable values.

α_1	α_2	α_S	α_L	K
34.52 μ	34.52 μ	25.2 μ	0.252 μ	0.08

Table 4. Capacitor and frequency calculation.

Figure 2b Resonant Frequency Calculation	Figure 2b Optimized Capacitor and Frequency Calculation	Figure 2a Resonant Frequency Calculation
$f = \frac{1}{2\pi\sqrt{L_1C}}$	$\omega^* = \frac{\sigma\sqrt{\alpha_1 + \alpha_S}(\alpha_2 + \alpha_L)}{\sqrt{\alpha_2}\sqrt{\alpha_L}}$ where σ as in (18) and $\omega = 2\pi f$ $Q^* = \frac{\alpha_2^2\alpha_1^2\omega^2 + \alpha_2^2 + 2\alpha_2\alpha_L + \alpha_L^2}{\alpha_S\omega^2(-K^2\alpha_2^2\alpha_1^2\omega^2 + \alpha_2^2\alpha_1^2\omega^2 + \alpha_2^2 + 2\alpha_2\alpha_L + \alpha_L^2)}$ where $Q = CR_S$ $C = 1.56$ nF $f = 803.6$ kHz	$f = \frac{1}{2\pi\sqrt{L_1C_1}} = \frac{1}{2\pi\sqrt{L_2C_2}}$ $C = 21.8$ pF $f = 6.78$ MHz
$C = 0.1$ μ F $f = 100$ kHz		

After calculating each configuration’s capacitor and frequency ($C-f$), we ran the SPICE AC analysis simulation. Figure 7 presents the results of the SPICE small-signal AC analysis. From these results, we can verify that our proposed design method for a single-capacitor circuit using the proposed optimized $C-f$ is able to obtain a high enough power level compared to that of the common dual-capacitor circuit using the idea of resonance. Furthermore, our proposed formula for obtaining an optimized $C-f$ can be used even if our single-capacitor circuit loses symmetry and does not use the idea of resonance.

3.4. Optimization during Changes in the Coupling Coefficient (K)

In this section, we conduct $C-f$ optimization while the coupling coefficient (K) changes, simulating distance variations between coils [16]. Our proposed optimization maintained a high-power level, which we verified by performing the $C-f$ computation in conjunction with the changes in K using the SPICE simulations. We used all the circuit component values from Table 1 except K , which we set as a free variable. Next, we compared the fixed $C-f$ ($C = 1.56$ nF and $f = 803.6$ kHz) with the optimized $C-f$ when the coupling coefficient K is swept from 0.03 to 0.5. Finally, we computed the optimized $C-f$ using Equations (15) and (16) and observed the results, presented in Figure 8. The fixed $C-f$ demonstrates power degradation as K increases. However, the optimized $C-f$ maintains the optimal power level, starting when the K coupling coefficient is larger than 0.1.

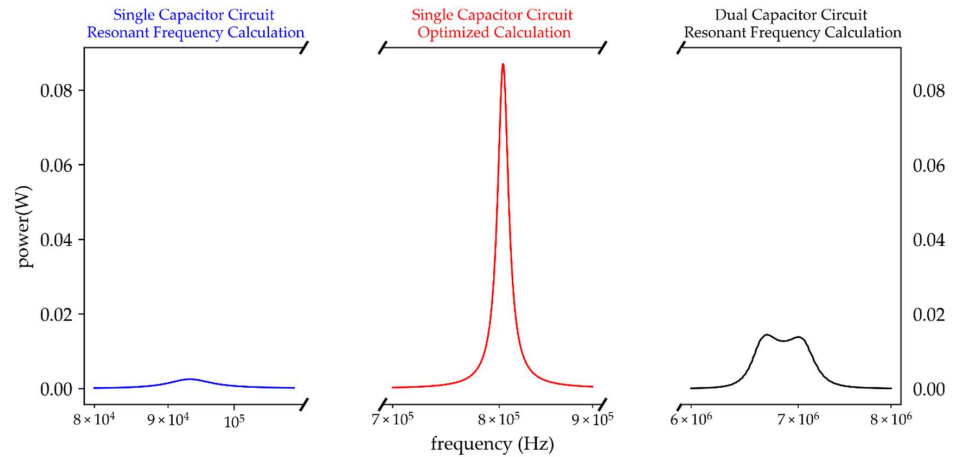


Figure 7. SPICE small-signal (1 volt) AC analysis result using the circuit based on component values in Tables 1 and 4. The capacitor and frequency are calculated using data in Table 4.

Table 5. List of K s with the optimized $C-f$ calculation results using Equations (15) and (16).

K	Optimized Capacitor (F)	Optimized Frequency (kHz)
0.03	2.35 n	653.86
0.08	1.56 n	803.60
0.13	40.4 p	5032.50
0.18	2.24 n	676.02
0.23	5.26 n	441.32
0.28	9 n	337.11
0.33	13.5 n	275.42
0.38	18.7 n	233.86
0.43	24.7 n	203.67
0.48	31.4 n	180.64

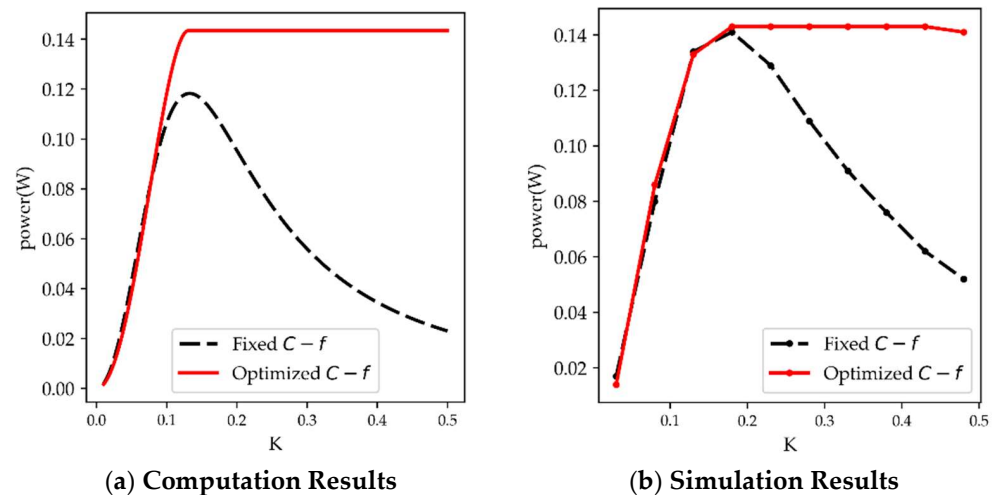


Figure 8. Effect of changes on the optimization results obtained from the calculation. The fixed $C-f$ label is where $C = 1.56$ nF and $f = 803.6$ kHz. The optimized $C-f$ label is where the $C-f$ are recalculated using Equations (15) and (16) during the changes in K : (a) 1000 samples were computed using Equations (15)–(17); (b) SPICE simulation results using range of K from Table 5.

The verification of the optimization conducted via the SPICE simulation using K 's value is shown in Table 5. We ran the simulations of AC analysis using the linear time

sweep with 1000 points and computed the optimized $C-f$ value results, which are shown in Table 5. The simulation plot is presented in Figure 8b. As shown in Figure 8a, power degradation occurs when K is between 0.1 and 0.2, and it further decreases when K reaches 0.5. However, when the $C-f$ is optimized, the R_L power shows a stable 0.14 Watt result.

3.5. Optimization during Changes in Load (R_L)

This section aims to verify our proposed optimization under different types of loads by observing the optimization results during changes in load (R_L). The optimization was performed using the topology shown in Figure 2b and the component setup listed in Table 1, with R_L being set as the free variable. To evaluate the performance of our proposed optimization, we compared the fixed $C-f$ ($C = 1.56$ nF and $f = 803.6$ kHz) with the optimized $C-f$ computed using Equations (15) and (16). The $C-f$ optimization was carried out while varying R_L from 10Ω to 100 k Ω (with 1000 data samples), and the results observed are plotted in Figure 9a. The computation results demonstrate that the fixed $C-f$ experiences power degradation as the R_L increases. In contrast, our proposed optimized $C-f$ shows a stable optimal result starting when R_L reaches 100Ω .

Table 6. List of R_L s with the optimized $C-f$ calculations, obtained using Equations (15) and (16).

R_L (Ω)	Optimized Capacitor (F)	Optimized Frequency (kHz)
10	0.211 μ	69.15
100	1.56 n	803.6
1k	68 p	3844.9
10k	9 p	10,527.37
100k	0.9 p	32,880.88

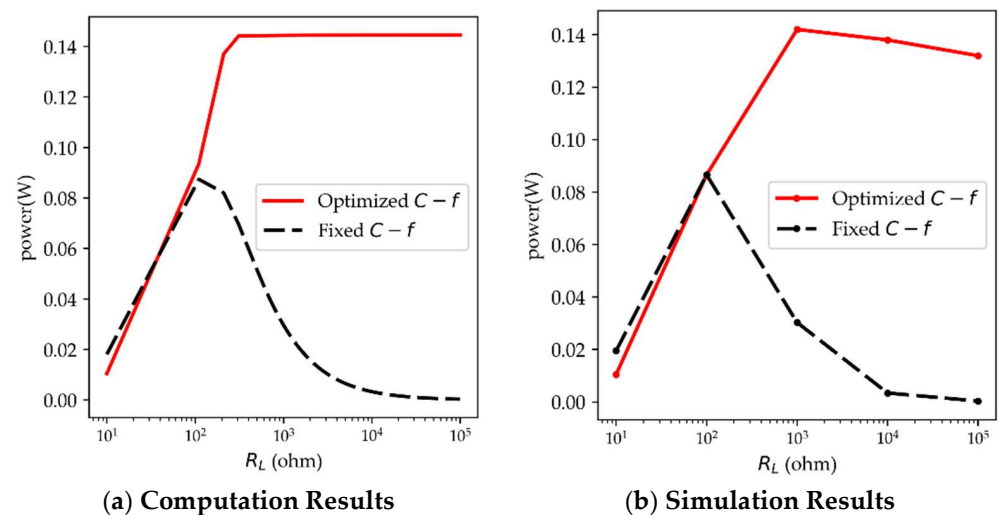


Figure 9. Effect of R_L changes on the optimization results obtained from the calculations. The fixed $C-f$ label is where $C = 1.56$ nF and $f = 803.6$ kHz. The optimized $C-f$ label is where the $C-f$ are optimized using Equations (15) and (16) during the changes in R_L : (a) 1000 samples were collected in the calculation process; (b) SPICE simulation results using range of R_L from Table 6.

The optimization verification was conducted in the SPICE simulation environment. To evaluate the effectiveness of our proposed optimization, we observed the R_L power consumption while fixing the $C-f$ at 1.56 nF and 803.6 kHz for different values of R_L , which are listed in Table 6. The simulations were ran through the AC analysis with a linear time sweep of 1000 points. The obtained results were compared with the optimized $C-f$ listed in Table 6, and the comparison results are presented in Figure 9b.

4. Discussion

This study was conducted in three phases to achieve a high-power level with the load (R_L). The first phase consisted of finding the system model for the primary-side single-capacitor WPT system, which was represented using the transfer function shown in Equation (2). In the second phase, steady-state analysis was performed, and the steady-state function R_L power ($p_{ss}(t)$) was obtained, as shown in Equation (9). The simulations with the initial condition presented in Figures 3 and 4 indicate that $p_{ss}(t)$ is a stable solution. Therefore, the average power of R_L can be calculated using the integration formula presented in Equations (10) and (11).

Optimization was carried out to maximize $p_{ss}(t)$ and to achieve a high-power level absorbed by R_L . Therefore, $p_{ss}(t)$ was set as the objective function. This study used the partial derivation of the capacitor and frequency to obtain the optimum point C^* , as in Equation (15), and f^* , as in Equation (16). The optimum function for R_L power can be obtained by substituting C^* and f^* into the objective function. A contour map is presented in Figure 10 to show a better perspective of the optimization results. In Figure 10, many peaks can be observed around the selection value for the capacitor and frequency. The R_L power obtained from the primary-circuit resonance frequency C - f is far smaller than that from the optimized C - f .

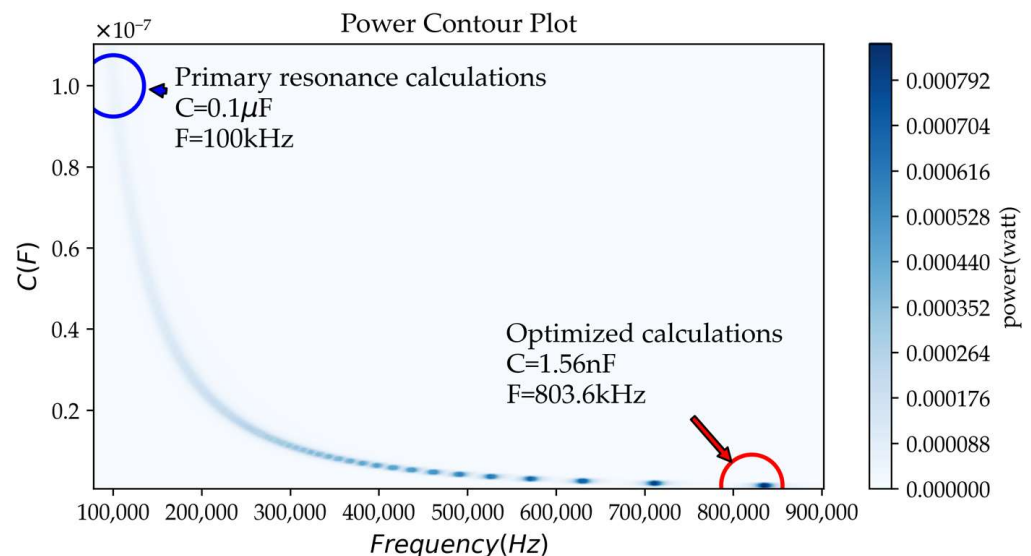


Figure 10. Power contour plot comparison from the calculation of C - f based on the primary-side resonant frequency and the optimization conditions.

This study compared the optimized C - f results with: (1) the single-capacitor primary-side resonant frequency calculation, and (2) the dual-capacitor circuit with the resonant frequency calculation. The comparison results show that the optimized C - f can deliver the highest power to the R_L , as shown in Figure 7. Next, this study presented the optimized C - f system behavior during coupling coefficient K or load R_L changes. The results are presented in Figures 8 and 9. Equations (15) and (16) were used to find the extremum point C and f , which can be used to maintain the optimal condition during changes to the K or R_L value.

Table 5 shows interesting results when the coupling coefficient $K = 0.13$. At this value of K , the optimized capacitor calculation is 40.4 pF, and the optimal frequency is 5.032 MHz. These optimized capacitor and frequency values are considered outliers compared to the other results in Table 5. Therefore, this study investigated further by conducting a numerical analysis using narrower values of K . The calculation was performed using Equations (15) and (16), and the results are presented in Figure 11a. The critical point for the frequency is calculated at 29.56 MHz when $K = 0.131$. Similar situations happen during

the numerical analysis with the narrower R_L (100 Ω –10 k Ω), as presented in Figure 11b. The critical point for the frequency is calculated at 26.47 MHz when $R_L = 268.46 \Omega$. Hence, these two situations are marked as important since they border the maximum power. Figure 11 shows the high-power area; in this area, we can select any critical points of a capacitor, frequency, coupling coefficient, or load resistor to suit the required condition.

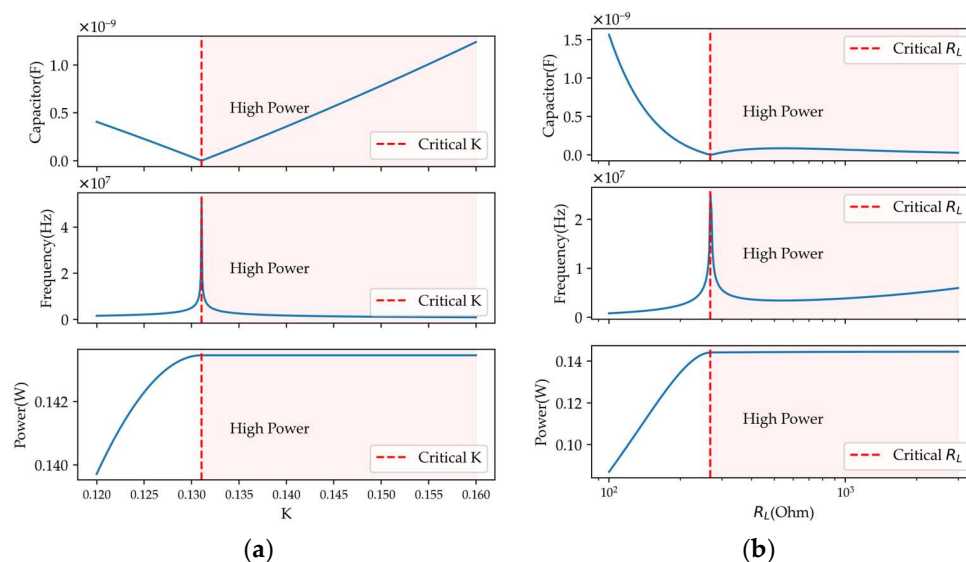


Figure 11. (a) Numerical analysis when $K = 0.10$ – 0.16 . Critical points are obtained at $K = 0.131$, $C = 1.171$ pF, and $f = 29.56$ MHz. (b) Numerical analysis when $R_L = 100 \Omega$ – $10 \text{ k}\Omega$. Critical points are obtained at $R_L = 268.46 \Omega$, $C = 1.44$ pF, and $f = 26.47$ MHz.

This study demonstrates that the critical point K or R_L can be determined from the numerical calculations. Additionally, the critical capacitors and frequency can maintain optimal conditions during coupling coefficient or load changes, allowing for optimal solutions to be selected based on system requirements. The optimization can be improved in future research by utilizing Equations (15) and (16) to obtain the critical values of the capacitor and frequency; then, constrained optimization techniques can be applied, such as the Karush–Kuhn–Tucker conditions [37], to satisfy the system requirement regarding the constrained condition in the frequency, capacitor, coupling coefficients, or load.

5. Conclusions

This study has presented a design method for a high-power WPT circuit without a capacitor on the secondary side. Although the circuit loses symmetry and prevents the use of the idea of resonance, it has been proven that the circuit transfers a high enough power level compared to a usual WPT circuit with capacitors on both sides that uses the idea of resonance. Additionally, the maximum power formula is obtained with the critical point formula for the capacitor and frequency in three general phases. The first and second phases demonstrate the transfer function calculations and the steady-state system's behavior in the form of a steady-state function. In the third phase, the steady-state function is maximized to obtain the optimum load power, capacitor, and frequency function. The numerical analysis comparison with the electronic circuit simulation is conducted as the verification method. The optimum point formula used to determine the capacitor and frequency proves that the optimal condition can be maintained during coupling coefficient or load changes. In the future, an experimental phase will be conducted that will consider two ferromagnetic cores in the L_1 and L_2 coils to decrease the total magnetic reluctance of the circuit, when using a lower magnetizing current.

Author Contributions: Conceptualization, S.R.A. and I.H.; methodology, S.R.A. and I.H.; software: S.R.A.; validation, E.S.; formal analysis, S.R.A. and I.H.; investigation, S.R.A. and I.H.; writing—original draft preparation, S.R.A., E.S., and T.H.; writing—review and editing, I.H., E.S., and T.H.; visualization, S.R.A.; supervision, I.H. All authors have read and agreed to the published version of the manuscript.

Funding: This research was supported by the Faculty of Computer Science, University of Brawijaya.

Data Availability Statement: Not applicable.

Acknowledgments: The authors would like to thank the members of the Control System Laboratory, University of Miyazaki.

Conflicts of Interest: The authors declare no conflict of interest.

References

1. Tesla, N. Apparatus for Transmitting Electrical Energy. U.S. Patent 1119732, 1 December 1914.
2. Kurs, A.; Karalis, A.; Moffatt, R.; Joannopoulos, J.D.; Fisher, P.; Soljacic, M. Wireless Power Transfer via Strongly Coupled Magnetic Resonances. *Science* **2007**, *317*, 83–86. [[CrossRef](#)] [[PubMed](#)]
3. Lecluyse, C.; Minnaert, B.; Kleemann, M. A Review of the Current State of Technology of Capacitive Wireless Power Transfer. *Energies* **2021**, *14*, 5862. [[CrossRef](#)]
4. Ullah, M.A.; Keshavarz, R.; Abolhasan, M.; Lipman, J.; Esselle, K.P.; Shariati, N. A Review on Antenna Technologies for Ambient RF Energy Harvesting and Wireless Power Transfer: Designs, Challenges and Applications. *IEEE Access* **2022**, *10*, 17231–17267. [[CrossRef](#)]
5. Mohammadnia, A.; Ziapour, B.M.; Ghaebi, H.; Khooban, M.H. Feasibility assessment of next-generation drones powering by laser-based wireless power transfer. *Opt. Laser Technol.* **2021**, *143*, 107283. [[CrossRef](#)]
6. Mulders, J.V.; Delabie, D.; Lecluyse, C.; Buyle, C.; Callebaut, G.; Perre, L.V.d.; Strycker, L.D. Wireless Power Transfer: Systems, Circuits, Standards, and Use Cases. *Sensors* **2022**, *22*, 5573. [[CrossRef](#)]
7. Jawad, A.M.; Nordin, R.; Gharghan, S.K.; Jawad, H.M.; Ismail, M. Opportunities and Challenges for Near-Field Wireless Power Transfer: A Review. *Energies* **2017**, *10*, 1022. [[CrossRef](#)]
8. Mou, X.; Sun, H. Wireless Power Transfer: Survey and Roadmap. In Proceedings of the 2015 IEEE 81st Vehicular Technology Conference (VTC Spring), Glasgow, UK, 11–14 May 2015.
9. Hui, S.Y.R.; Zhong, W.; Lee, C.K. A Critical Review of Recent Progress in Mid-Range Wireless Power Transfer. *IEEE Trans. Power Electron.* **2014**, *29*, 4500–4511. [[CrossRef](#)]
10. Yamaguchi, K.; Hirata, T.; Hodaka, I. High Power Wireless Power Transfer Driven by Square Wave Inputs. In Proceedings of the International Conference on Genetic and Evolutionary Computing, GEC 2015, Advances in Intelligent Systems and Computing, Yangon, Myanmar, 26–28 August 2015.
11. Wei, X.; Wang, Z.; Dai, H. A Critical Review of Wireless Power Transfer via Strongly Coupled Magnetic Resonances. *Energies* **2014**, *7*, 4316–4341. [[CrossRef](#)]
12. Chen, L.; Liu, S.; Zhou, Y.C.; Cui, T.J. An Optimizable Circuit Structure for High-Efficiency Wireless Power Transfer. *IEEE Trans. Ind. Electron.* **2013**, *60*, 339–349. [[CrossRef](#)]
13. Mude, K.N.; Aditya, K. Comprehensive review and analysis of two-element resonant compensation topologies for wireless inductive power transfer systems. *Chin. J. Electr. Eng.* **2019**, *5*, 14–31. [[CrossRef](#)]
14. Zhang, W.; Mi, C.C. Compensation Topologies of High-Power Wireless Power Transfer Systems. *IEEE Trans. Veh. Technol.* **2015**, *65*, 4768–4778. [[CrossRef](#)]
15. Bertoluzzo, M.; Giacomuzzi, S.; Sieni, E. Automatic Optimization of the Compensation Networks of a Wireless Power Transfer System. *Energies* **2020**, *13*, 5298. [[CrossRef](#)]
16. Li, Y.; Jiang, S.; Liu, X.-L.; Li, Q.; Dong, W.-H.; Liu, J.-M.; Ni, X. Influences of Coil Radius on Effective Transfer Distance in WPT System. *IEEE Access* **2019**, *7*, 125960–125968. [[CrossRef](#)]
17. Zulauf, G.; Rivas-Davila, J.M. Single-Turn Air-Core Coils for High-Frequency Inductive Wireless Power Transfer. *IEEE Trans. Power Electron.* **2020**, *35*, 2917–2932. [[CrossRef](#)]
18. Sampath, J.; Alphones, A.; Shimasaki, H. Coil design guidelines for high efficiency of wireless power transfer (WPT). In Proceedings of the 2016 IEEE Region 10 Conference (TENCON), Singapore, 22–25 November 2016.
19. Jiang, C.; Chau, K.T.; Liu, C.; Lee, C.H.T. An Overview of Resonant Circuits for Wireless Power Transfer. *Energies* **2017**, *10*, 894. [[CrossRef](#)]
20. Niu, W.; Gu, W.; Chu, J. Analysis and experimental results of frequency splitting of underwater wireless power transfer. *J. Eng.* **2017**, *7*, 385–390. [[CrossRef](#)]
21. Wang, J.; Leach, M.; Lim, E.G.; Wang, Z.; Huang, Y. Investigation of magnetic resonance coupling circuit topologies for wireless power transmission. *Microw. Opt. Technol. Lett.* **2019**, *61*, 1755–1763. [[CrossRef](#)]
22. Truong, B.D. Investigation on power optimization principles for series-configured resonant coupled wireless power transfer systems. *AEU Int. J. Electron. Commun.* **2019**, *106*, 67–81. [[CrossRef](#)]

23. Beh, T.C.; Kato, M.; Imura, T.; Oh, S.; Hori, Y. Automated Impedance Matching System for Robust Wireless Power Transfer via Magnetic Resonance Coupling. *IEEE Trans. Ind. Electron.* **2013**, *60*, 3689–3698. [[CrossRef](#)]
24. Andoh, H.; Tsuzuki, K.; Oikawa, D.; Sugiura, T.; Tsukamoto, T.; Maezawa, K. Study on impedance matching and maximum wireless power transfer efficiency of circuits with investigated coupling based on simplified S-matrix. *IEICE Electron. Express* **2019**, *16*, 20190156. [[CrossRef](#)]
25. Frivaldsky, M.; Jaros, V.; Spanik, P.; Pavelek, M. Control system proposal for detection of optimal operational point of series-series compensated wireless power transfer system. *Electr. Eng.* **2020**, *102*, 1423–1432. [[CrossRef](#)]
26. Akbar, S.R.; Hodaka, I. A Design Approach to Wireless High-Power Transfer to Multiple Receivers with Asymmetric Circuit. *Int. J. Circuits Syst. Signal Process.* **2021**, *15*, 125–134. [[CrossRef](#)]
27. Yamaguchi, K.; Hirata, T.; Hodaka, I. A general method to parameter optimization for highly efficient wireless power transfer. *Int. J. Electr. Comput. Eng.* **2016**, *6*, 3217–3221.
28. Ali, A.; Najib, M.; Yasin, M.; Jusoh, M.; Hambali, N.A.M.A.; Rafidah, S.; Rahim, A. Optimization of wireless power transfer using artificial neural network: A review. *Microw. Opt. Technol. Lett.* **2020**, *62*, 651–659. [[CrossRef](#)]
29. Bai, T.; Mei, B.; Zhao, L.; Wang, X. Machine Learning-Assisted Wireless Power Transfer Based on Magnetic Resonance. *IEEE Access* **2019**, *7*, 109454–109459. [[CrossRef](#)]
30. Akbar, S.R.; Setiawan, E.; Hirata, T.; Yamaguchi, K.; Hodaka, I. The Frequency Response and Steady-State analysis on Wireless Power Transfer using Square Wave Input. In Proceedings of the 6th International Conference on Sustainable Information Engineering and Technology 2021, Malang, Indonesia, 13–14 September 2021.
31. Setiawan, E.; Hirata, T.; Hodaka, I. Accurate Symbolic Steady State Modeling of Buck Converter. *Int. J. Electr. Comput. Eng.* **2017**, *7*, 2374–2381. [[CrossRef](#)]
32. Barman, S.D.; Reza, A.W.; Kumar, N.; Karim, M.E. Wireless powering by magnetic resonant coupling: Recent trends in wireless power transfer system and its applications. *Renew. Sustain. Energy Rev.* **2015**, *51*, 1526–1552. [[CrossRef](#)]
33. Abner Ramirez, G.C. Reduced-sample numerical Laplace transform for transient and steady-state simulations: Application to networks involving power electronic converters. *Int. J. Electr. Power Energy Syst.* **2019**, *109*, 480–494. [[CrossRef](#)]
34. Hirata, T.; Yamaguchi, K.; Hodaka, I. A symbolic equation modeler for electric circuits. *ACM Commun. Comput. Algebra* **2015**, *49*, 1932–2240. [[CrossRef](#)]
35. Wings, J.; Rylander, T.; Petersson, C.; Ekman, C.; Johansson, L.-A.; McKelvey, T. Multi-Objective Optimization of Wireless Power Transfer Systems with Magnetically Coupled Resonators and Nonlinear Loads. *Progress Electromagn. Res. B* **2019**, *83*, 24–42. [[CrossRef](#)]
36. Wolovich, W.A. *Automatic Control Systems: Basic Analysis and Design*; Oxford University Press, Inc.: Oxford, UK, 1993.
37. Haeser, G.; Ramos, A. Constraint Qualifications for Karush–Kuhn–Tucker Conditions in Multiobjective Optimization. *J. Optim. Theory Appl.* **2020**, *187*, 469–487. [[CrossRef](#)]

Disclaimer/Publisher’s Note: The statements, opinions and data contained in all publications are solely those of the individual author(s) and contributor(s) and not of MDPI and/or the editor(s). MDPI and/or the editor(s) disclaim responsibility for any injury to people or property resulting from any ideas, methods, instructions or products referred to in the content.